Journal of Power Sources 195 (2010) 1–10

Contents lists available at ScienceDirect

Journal of Power Sources

journal homepage: www.elsevier.com/locate/jpowsour

Analysis of the kinetics of methanol oxidation in a porous Pt–Ru anode

Yan-Ping Sun[a,*], Lei Xing[a], Keith Scott[b]

[a] Chemical Engineering Department, Taiyuan University of Technology, Shanxi 030024, China
[b] School of Chemical Engineering and Advanced Materials, Merz Court, University of Newcastle, Newcastle upon Tyne NE1 7RU, UK

ARTICLE INFO

Article history:
Received 5 May 2009
Received in revised form 14 July 2009
Accepted 14 July 2009
Available online 22 July 2009

Keywords:
DMFC
Porous anode
Methanol oxidation
Dual-site mechanism
Macro-kinetics
Mathematic model

ABSTRACT

A kinetic model of a porous Pt–Ru anode for methanol oxidation is presented. It was based on the dual-site mechanism for methanol oxidation and used to predict anode performance and the influence of species adsorption on the overall oxidation (macro-) kinetics. The performance of the porous Pt–Ru anode depended on the parameters of the intrinsic chemical kinetics of methanol oxidation and physical parameters such as electrode thickness, surface area, effective diffusion and charge transfer coefficients and concentration of methanol and temperature. The model was solved by using the finite difference method with a subroutine for solving a set of nonlinear algebraic equations in each step. Surface coverage ratio distributions of adsorbed species, effectiveness of the porous electrode and macro-polarisation curves were obtained. The simulated polarisation curves were compared to experimental polarisation data for methanol oxidation on Pt–Ru porous anodes at different temperatures and methanol concentrations. The intrinsic kinetic parameters were regressed from the corresponding experimental data. The predicted polarisation curves calculated by the model, were consistent with experimental polarisation data at lower current densities. The departure of experimental data from the predicted polarisation curves at high concentration and high apparent current densities was believed to be due to two-phase flow in the electrode.

1. Introduction

The direct methanol fuel cell (DMFC) has a lower power density, a larger voltage loss and lower limiting current than the corresponding hydrogen polymer electrolyte membrane fuel cells (PEMFCs). There are considerable differences in reported DMFC performances; since issues of catalyst, membrane, kinetics and transport processes arising with the DMFC are more complex than those from hydrogen PEMFCs [1–3].

A typical PEMFC is made up of a membrane electrode assembly (MEA), consisting of the membrane, electrocatalyst layers and reactant diffusion layers, and flow channels incorporating current collectors. Important components for cell performance are the porous electrodes in the MEA where electrochemical reactions occur (see Fig. 1). Unlike, hydrogen PEMFCs, a dominating kinetic resistance (polarisation) in the DMFC is at the anode due to sluggish oxidation of methanol [1–4].

Generally porous electrode structures are used to support high current densities at low polarisation, although typically current and overpotential are non-uniform due to the influence of mass and charge transfer in the structure [5–7]. Generalized mathematical models of porous; three-dimensional electrodes have been developed in previous papers [7–11]. For isothermal systems the models describe the coupled potential and concentration distributions in the porous or packed bed electrodes at steady state.

Even though the mechanism of methanol electro-oxidation on Pt–Ru catalyst in the DMFC is not fully understood, researchers have come to a common understanding, namely that simple Tafel or B–V equations are unable to represent the intrinsic methanol oxidation kinetics and a dual-site mechanism on Pt–Ru catalyst surfaces has been accepted [12–16]. Consequently for a model of the observed or macro-kinetics of the DMFC anode it is important to include the appropriate dual-site mechanism of methanol oxidation.

A few models have been developed for unit cells or the anode of the DMFC. Meyers and Newman developed a comprehensive model which describes the thermodynamics, transport phenomena, and electrode kinetics of the system in DMFC [4]. García et al. presented a semi-analytical model which can be solved rapidly so that it is suitable for inclusion in real-time system level DMFC simulations [17]. Nordlund and Lindbergh adopted a porous model with agglomerates and kinetic equations based on surface coverage to study the influence of porous structure on the DMFC anode [18]. Scott and Argyropoulos developed a one-dimensional model of the current distribution in the anode of DMFC, which can be solved analytically [19]. However, combina-

* Corresponding author. Tel.: +86 351 6010070; fax: +86 351 6041237.
E-mail addresses: ypsun@tyut.edu.cn (Y.-P. Sun), xinglei1314@gmail.com (L. Xing), k.scott@ncl.ac.uk (K. Scott).

0378-7753/$ – see front matter © 2009 Elsevier B.V. All rights reserved.
doi:10.1016/j.jpowsour.2009.07.028

Nomenclature

a	specific electrode area (m^{-1})
C	dimensionless concentration
c	concentration (mol m^{-3})
D_0	diffusion coefficient (m^2 s^{-1})
D_e	effective diffusion coefficient (m^2 s^{-1})
E	overpotential (V)
F	Faraday constant (C mol^{-1})
J	dimensionless current density
J_{al}	dimensionless adsorption limiting current density
j	current density (A m^{-2})
j_0	exchange current density (A m^{-2})
j_{al}	adsorption limiting current density (A m^{-2})
k_4	surface rate constant (mol m^{-2} s^{-1})
l	thickness of porous anode (m)
N_M	flux of methanol (mol m^{-2} s^{-1})
n	number of electrons involved in reaction
R_g	universal gas constant (J mol^{-1} K^{-1})
R	apparent reaction rate (mol m^{-2} s^{-1})
r_4	surface reaction rate (mol m^{-2} s^{-1})
s	dimensionless modulus, $aj_0l^2/(nFD_ec_M^0)$
T	temperature (K)
X	dimensionless distance
x	distance (m)

Greek letters

β	$(1-\beta_3)F/RT = (1-\beta_4)F/RT$ (V^{-1})
ε	porosity
θ	coverage ratio
κ_e	effective conductivity (Ω^{-1} m^{-1})
μ	dimensionless modulus, ν^2/Φ^0
ν^2	dimensionless parameter, $aj_0l^2\beta/\kappa_e$
ξ	effectiveness
ϕ^0	potential of open-circuit (V)
ϕ^l	potential of electrolyte (V)
ϕ^m	potential of matrix (V)
Ψ	dimensionless relative overpotential, $\Phi/\beta E^0$

Subscripts

ads	adsorbed
e	effective
i	species i
loc	local state
M	methanol
T	total or apparent state

Superscripts

0	at the boundary of the diffusion layer $X = 1$

tion of the dual-site methanol oxidation model with the material and charge transport behaviour of the porous DMFC anode has not been addressed.

In the present model, the dual-site methanol oxidation mechanism [15,16] was combined with material and charge balances [7–11] to simulate the porous anode behaviour and predict the effect of methanol concentration and temperature on anode polarisation; thereby providing a useful tool for theoretical analysis of macro-kinetics.

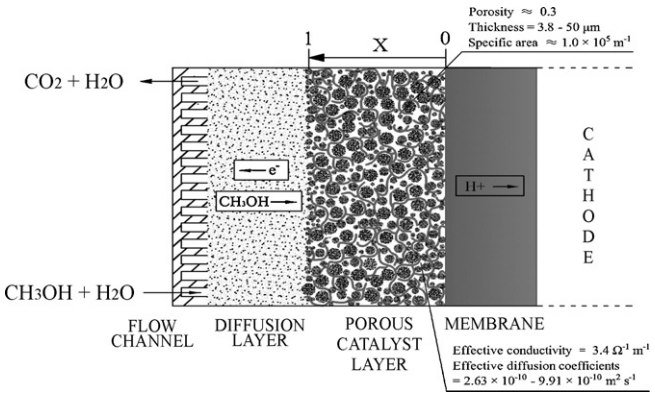

Fig. 1. Scheme of the porous anode in DMFC.

2. Model equations for macro-kinetics

Carbon dioxide is produced from methanol electrochemical oxidation at the anode surface in acidic solution, in the DMFC [1,20,21].

$$CH_3OH + H_2O \rightarrow CO_2 + 6H^+ + 6e^- \quad (1)$$

The formation of CO_2 bubble is related to factors, such as local reaction conditions, solubility, surface tension, pore structure, etc. and may raise issues associated with transport phenomena of two-phase flow. By choosing appropriate conditions, it is possible for nucleation of CO_2 to take place in the diffusion layer away from the active layer of porous anode or to be limited to a small region of the active layer [20,21], which will be favourable for anode performance. In this model, the influence of CO_2 bubbling is omitted, although it is indeed difficult to avoid the effect of two-phase flow in the diffusion layer and flow channel to analyse the whole DMFC (Fig. 1).

The main task in the mathematic model of the porous anode was to introduce the intrinsic kinetic expression for methanol oxidation into the charge and material balances; which are described below.

2.1. Intrinsic kinetics expression

The intrinsic kinetics of methanol electro-oxidation on Pt–Ru catalyst has been studied in detail [15]. The assumed reaction steps (from (A.1)–(A.4)) and the corresponding rate expressions (from (R.1)–(R.4)) are listed in Table 1. There is a series of reactions for key components of methanol (M). At a steady state, the rates of these reaction steps should be equal, i.e. $r_1 = r_2 = r_4$, and only one is needed to represent the total reaction rate of the series. In this paper, the expression for r_4 for the last step in the series, involving information of all elementary steps (including the parallel OH^- adsorption), was selected as the intrinsic kinetics expression. The last step is a surface reaction which is believed to occur on both the Pt and Ru sites depending upon the hydroxyl ion. Two cases of kinetics, have been developed previously according to the dual-site mechanism, depending upon whether or not surface coverage of OH on Pt site could be neglected [14–16]. Since the modeling procedures are similar for both cases, $OH_{ads,Ru}$ was mainly used for modeling in this paper.

The surface rate expression (mol m^{-2} s^{-1}) of the last reaction step (Eq. (A.4) in Table 1) can be written as:

$$-r_4 = k_4\theta_{OH,Ru}\theta_{CO}\ \exp(\beta E) \quad (2)$$

where k_4 is the rate constant, $\theta_{OH,Ru}$ and θ_{CO} are the coverage ratios of OH_{ads} at Ru sites and CO_{ads} at Pt sites respectively, $\beta = (1-\beta_3)F/RT = (1-\beta_4)F/RT$ [15,16], and E is the overpotential.

Table 1
The reaction steps for methanol oxidation and their rate expressions and surface coverage of intermediate species according to the dual-site mechanism on a Pt–Ru anode [15].

Elemental steps		Rate expressions	
$CH_3OH \underset{k'_1}{\overset{k_1}{\Leftrightarrow}} CH_3OH_{ads}$	(A.1)	$-r_1 = k_1 C_M(1-\theta_{OH,Pt}-\theta_{CO}-\theta_M) - k'_1\theta_M - k_2\theta_M\ e^{(\alpha_2 FE/RT)}$	(R.1)
$CH_3OH_{ads} \overset{k_2}{\Rightarrow} CO_{ads} + 4H^+ + 4e^-$	(A.2)	$-r_2 = k_2\theta_M e^{(\alpha_2 FE/RT)} - k_{4,1}\theta_{OH,Pt}\theta_{CO}\ e^{((1-\beta_3)FE/RT)} - k_{4,2}\theta_{OH,Ru}\theta_{CO}\ e^{((1-\beta_4)FE/RT)}$	(R.2)
$H_2O \underset{k'_{3,1}}{\overset{k_{3,1}}{\Leftrightarrow}} OH_{ads,Pt} + H^+ + e^-$	(A.3.1)	$-r_{3,1} = k_{3,1}a_{H_2O}(1-\theta_{OH,Pt}-\theta_{CO}-\theta_M)\ e^{((1-\beta_3)FE/RT)} - k'_{3,1}\theta_{OH,Pt}\theta_{CO}\ e^{((-\beta_3)FE/RT)}$	(R.3.1)
$H_2O \underset{k'_{3,2}}{\overset{k_{3,2}}{\Leftrightarrow}} OH_{ads,Ru} + H^+ + e^-$	(A.3.2)	$-r_{3,2} = k_{3,2}a_{H_2O}(1-\theta_{OH,Ru})\ e^{((1-\beta_3)FE/RT)} - k'_{3,2}\theta_{OH,Ru}\theta_{CO}\ e^{((-\beta_3)FE/RT)}$	(R.3.2)
$CO_{ads} + (OH_{ads,Pt} + OH_{ads,Ru}) \underset{k_{4,2}}{\overset{k_{4,1}}{\Rightarrow}} CO_2 + H^+ + e^-$	(A.4)	$-r_4 = k_{4,1}\theta_{OH,Pt}\theta_{CO}\ e^{((1-\beta_3)FE/RT)} + k_{4,2}\theta_{OH,Ru}\theta_{CO}\ e^{((1-\beta_4)FE/RT)}$	(R.4)

Surface coverage of different intermediate species in two different cases

Case A ($\theta_{OH,Pt}=0$)	Case B ($\theta_{OH,Pt}\neq 0$)
$\theta_{CO} = 1-\theta_M-\left(\frac{k'_1\theta_M}{k_1 c_M}\right)-\left(\frac{k_2\theta_M\ e^{(\alpha_2 FE/RgT)}}{k_1 c_M}\right)$	$\theta_{CO} = 1-\theta_{OH,Pt}-\theta_M-\left(\frac{k'_1\theta_M}{k_1 c_M}\right)-\left(\frac{k_2\theta_M\ e^{(\alpha_2 FE/RgT)}}{k_1 c_M}\right)$
$\theta_{CO} = \frac{k_2\theta_M\ e^{(\alpha_2 FE/RgT)}}{k_{4,2}\theta_{OH,Ru}\ e^{((1-\beta_4)FE/RgT)}}$	$\theta_{CO} = \frac{k_2\theta_M\ e^{(\alpha_2 FE/RgT)}}{k_{4,1}\theta_{OH,Pt}\ e^{((1-\beta_4)FE/RgT)}+k_{4,2}\theta_{OH,Ru}\ e^{((1-\beta_4)FE/RgT)}}$
$\theta_{CO} = \frac{k_{3,2}\ e^{((1-\beta_3)FE/RgT)}-k_{3,2}\theta_{OH,Ru}\ e^{((1-\beta_3)FE/RgT)}-k'_{3,2}\theta_{OH,Ru}\ e^{((-\beta_3)FE/RgT)}}{k_{4,2}\theta_{OH,Ru}\ e^{((1-\beta_4)FE/RgT)}}$	$\theta_{CO} = \frac{k_{3,1}(1-\theta_{OH,Pt}-\theta_M)\ e^{((1-\beta_3)FE/RgT)}-k'_{3,1}\theta_{OH,Pt}\ e^{((-\beta_3)FE/RgT)}}{k_{3,1}\ e^{((1-\beta_3)FE/RgT)}+k_{4,1}\theta_{OH,Pt}\ e^{((1-\beta_4)FE/RgT)}}$
	$\theta_{CO} = \frac{k_{3,2}(1-\theta_{OH,Ru})e^{((1-\beta_3)FE/RgT)}-k'_{3,2}\theta_{OH,Ru}\ e^{((-\beta_3)FE/RgT)}}{k_{4,2}\theta_{OH,Ru}\ e^{((1-\beta_4)FE/RgT)}}$

Note: $c_M = c_M^0 C_M$, $E = E^0\Psi$.

The surface current density ($A\,m^{-2}$) will be

$$j = \frac{nF}{s_i}(-r_4) = \frac{nF}{s_i}k_4\theta_{OH,Ru}\theta_{CO}\ \exp(\beta E) \tag{3}$$

where s_i is the stoichiometric coefficient in the electrode reaction, and n is the number of electrons involved in a reaction.

With $s_i = 1$, we have

$$j = j_0\theta_{OH,Ru}\theta_{CO}\ \exp(\beta E) \tag{4}$$

where $j_0 = nFk_4$.

Eq. (4) describes the behaviour of activation polarisation at the interfacial surface of pores in the anode.

It should be noted that the expressions of $\theta_{OH,Ru}$ and θ_{CO} are complex, which meant that the intrinsic kinetics expression used to analyse the Pt–Ru porous anode was nonlinear. To obtain the values of $\theta_{OH,Ru}$ and θ_{CO} a set of nonlinear algebraic equations [15] listed in Table 1 were solved. Two cases for adsorption of OH are presented in the table.

2.2. Mass and charge balances

Transfer processes in a macro-reaction system can form spatial distributions of reaction kinetic parameters, namely, the mass and energy fields [6,10]. The fields in a three-dimensional electrode can be described mathematically by mass and energy balances in a differential volume of the system [7–11].

$$\nabla\cdot\vec{N}_i = ar_i = -\frac{s_i}{n_i F}aj(E, c_i) \tag{5}$$

$$\nabla\cdot\vec{j} = aj(E, c_i) = \frac{n_i F}{s_i}ar_i \tag{6}$$

where $\vec{N}_i$ is the flux density of species i ($mol\,m^{-2}\,s^{-1}$), $\nabla\cdot\vec{N}_i$ is the divergence of $\vec{N}_i$ ($mol\,m^{-3}\,s^{-1}$), $\nabla\cdot\vec{j}$ is the divergence of $\vec{j}$ ($A\,m^{-3}$), c_i and r_i are the concentration of species i ($mol\,m^{-3}$) and rate of reactant of species i ($mol\,m^{-2}\,s^{-1}$) respectively and a is the specific area of the electrode (m^{-1}).

The source term $j(E,c_i)$ in Eqs. (5) and (6) is determined by the reaction mechanism. For the porous anode of the DMFC, when there is excess water, the mass balance will be only for the key component methanol as the influence of mass transfer of products can be neglected. Also the energy balance will only consider charge and not heat because an isothermal electrochemical system is assumed. A key point of this work was to use the intrinsic kinetic expression Eq. (2) as the chemical source term for the mass and charge balances [7,10,11].

2.2.1. Mass balance in a differential volume

We assume diffusion as the only mass transport mechanism of methanol in the porous structure, which is characterised by the effective diffusion coefficient D_e ($m^2\,s^{-1}$); according to Fick's Law,

$$\vec{N}_M = -D_e\nabla c_M \tag{7}$$

where ∇c_M is the concentration gradient of methanol.

For a one-dimensional slab of porous electrode, we substitute Eq. (7), Eq. (2) or Eq. (4) into Eq. (5),

$$\frac{d^2c_M}{dx^2} = \frac{a}{D_e}k_4\theta_{OH,Ru}\theta_{CO}\ \exp(\beta E) = \frac{aj_0}{nFD_e}\theta_{OH,Ru}\theta_{CO}\ \exp(\beta E) \tag{8}$$

which describes the effect of concentration changes on activation polarisation in the porous anode.

Assuming the flux of methanol through the membrane can be neglected and that both diffusion in the diffusion layer and two-phase flow in the flow channel do not influence the reaction rate, the concentration of methanol was constant c_M^0 at the boundary between the diffusion layer and active layer. The thickness of the porous active layer was, l, then the boundary conditions for the second order differential equation was

$$\begin{aligned} &x = 0, \quad \frac{dc_M}{dx} = 0 \quad \text{(at membrane)};\\ &x = l, \quad c_M = c_M^0 \quad \text{(at the boundary of the diffusion layer)} \end{aligned} \tag{9}$$

Therefore the flux density of methanol into the active layer, the macro-reaction rate R, was

$$N_M = R = -D_e\left(\frac{dc_M}{dx}\right)_{x=l} \tag{10}$$

and the flux density of charge, the total current density, was

$$j_T = -nFD_e\left(\frac{dc_M}{dx}\right)_{x=l} \tag{11}$$

2.2.2. Charge balance in a differential volume

Assuming the ohmic resistance of the electrode matrix can be neglected, charge transport in the electrolyte of the porous struc-

ture, which was characterised by the effectiveness conductivity κ_e (Ω^{-1} m^{-1}), was given by Ohm's law:

$$\vec{j} = -\kappa_e \nabla \phi^l \tag{12}$$

where ϕ^l is the potential of the electrolyte phase (V), $\nabla\phi^l$ is the gradient of potential.

The overpotential, E is written as $E = \phi^m - \phi^l - \phi^0$ [18], where both. ϕ^m is the potential of the solid electrode phase and, ϕ^0 is the open-circuit value can be considered as constant. Substituting Eq. (12) into Eq. (6), the differential charge balance to describe the potential field in the porous anode becomes a nonlinear Poisson equation

$$\nabla^2 E = \frac{a}{\kappa_e} j \tag{13}$$

For a slab of porous electrode, we deploy the Laplacian in Eq. (13) and substitute Eq. (2) or (4) into Eq. (13),

$$\frac{d^2E}{dx^2} = \frac{a}{\kappa_e} nFk_4 \theta_{OH,Ru}\theta_{CO}\ \exp(\beta E) = \frac{aj_0}{\kappa_e}\theta_{OH,Ru}\theta_{CO}\ \exp(\beta E) \tag{14}$$

which describes the effect of the ionic resistance on activation polarisation in the porous anode.

The overpotential is assumed constant E^0 at the boundary between the diffusion layer and active layer, and the boundary conditions of the second order differential equation will be

$$\begin{aligned} &x = 0, \quad \frac{dE}{dx} = 0 \quad \text{(at membrane)} \\ &x = l, \quad E = E^0 \quad \text{(at the border of diffusion layer)} \end{aligned} \tag{15}$$

Therefore the charge flux density coming from the active layer, i.e. the total current density j_T, is

$$j_T = -\kappa_e \left(\frac{dE}{dx}\right)_{x=l} \tag{16}$$

and the flux density of methanol going into the active layer, the macro-reaction rate R, is

$$N_M = R = -nF\kappa_e \left(\frac{dE}{dx}\right)_{x=l} \tag{17}$$

Coupling Eqs. (8) and (9) with Eqs. (14) and (15), we obtain a set of nonlinear differential equations which describes the coupled concentration and overpotential distributions along the lateral direction x of the porous electrode, i.e. the mathematic model of macro-kinetics with a dual-site mechanism for the Pt–Ru porous anode in DMFC.

2.3. Generalizing and decoupling the model equations

Generalizing the model equations [7–11], by defining dimensionless variables $C_M = c_M/c_M^0$, $\Phi = \beta E$, $X = x/l$, the dimensionless theoretical expressions and dimensionless parameters can be obtained as follows. Moreover, to improve the model and the precision of the solution, the boundary condition for overpotential at $X = 1$ is normalized by defining a relative dimensionless overpotential $\Psi = \Phi/\beta E^0 = \Phi/\Phi^0$, we have

$$\begin{aligned} \frac{d^2C_M}{dX^2} &= s \cdot \theta_{OH,Ru}\theta_{CO}\ \exp(\beta E^0 \Psi), \\ \frac{d^2\Psi}{dX^2} &= \mu \cdot \theta_{OH,Ru}\theta_{CO}\ \exp(\beta E^0 \Psi) \end{aligned} \tag{18}$$

with boundary conditions:

$$\begin{aligned} &X = 0, \quad \frac{dC_M}{dX} = 0, \quad \frac{d\Psi}{dX} = 0 \\ &X = 1, \quad C_M = 1, \quad \Psi = 1 \end{aligned}$$

The dimensionless modulus in Eq. (18), $s = aj_0l^2/nFD_ec_M^0$, characterises the resistances of mass transport in the porous anode. The dimensionless modulus $\mu = \nu^2/\beta E^0 = \nu^2/\Phi^0$, where $\nu^2 = aj_0l^2\beta/\kappa_e$, characterises the relative resistance of charge transport when applying different overpotentials at the boundary $X = 1$. Thus, a set of the generalizing model Eq. (21) can be used to theoretically analyze the effects of the coupled activation, concentration and ohmic polarisation on overall polarisation in the porous anode of the DMFC.

Decoupling Eq. (21), we have

$$\frac{d^2C_M}{dX^2} = \frac{s}{\mu}\frac{d^2\Psi}{dX^2} \tag{19}$$

With the boundary conditions we obtain from Eq. (19)

$$(C_M - 1) = \frac{s}{\mu}(\Psi - 1) \tag{20}$$

Substituting Eq. (20) into Eq. (18), we have

$$\frac{d^2C_M}{dX^2} = s \cdot \theta_{OH,Ru}\theta_{CO}\ \exp\left\{\beta E^0\left[1 + \frac{\mu}{s}(C_M - 1\right]\right\} \tag{21}$$

$$\begin{aligned} &X = 0, \quad \frac{dC_M}{dX} = 0 \\ &X = 1, \quad C_M = 1 \end{aligned}$$

where $\theta_{OH,Ru}$ or θ_{CO} is a function of C_M only.

Solution of Eq. (21) thus gives the concentration distribution in the anode and from Eq. (20) the potential distribution also can be obtained.

2.4. Polarisation curves and effectiveness factors of the porous anode

According to Ohm's law, the local current density at a lateral distance x is

$$j_{loc} = -nFD_e\frac{dc_M}{dx} = -\kappa_e\frac{dE}{dx} \tag{22}$$

The dimensionless current density is thus defined as

$$J_{loc} = -nF\frac{1}{s}\frac{dC_M}{dX} = -\frac{1}{\nu^2}\frac{d\Phi}{dX} = -\frac{1}{\mu}\frac{d\Psi}{dX} \tag{23}$$

From expressions of s and μ (or ν^2), we obtain the relation between j and J, i.e.

$$J = \frac{j}{aj_0l} = \frac{j}{aln\,Fk_4} \tag{24}$$

Hence Eqs. (22) and (23) describe the distributions of current density and the total current density, i.e. the apparent (macro-) current density of a porous electrode with a thickness l, will be

$$\begin{aligned} j_T = aj_0lJ_T &= -\kappa_e\left(\frac{dE}{dx}\right)_{x=l} = -\frac{\kappa_eE^0}{l}\left(\frac{d\Psi}{dX}\right)_{X=1} \\ &= -\frac{\kappa_e\Phi^0}{\beta l}\left(\frac{d\Psi}{dX}\right)_{X=1} \end{aligned} \tag{25}$$

where the relation of E^0–j_T describes the apparent (macro-) polarisation curve of the porous anode and the relation of Φ^0–J_T the apparent dimensionless polarisation curve.

The corresponding apparent (macro-) reaction rate can be written as

$$R = \frac{j_T}{nF} = \frac{aj_0l}{nF}J_T = -D_e\left(\frac{dc_M}{dx}\right)_{x=l} = -\frac{D_ec_M^0}{l}\left(\frac{dC_M}{dx}\right)_{X=1} \tag{26}$$

Introducing the effectiveness factor of the porous anode to scale the impact of parameters such as a, l, D_e and κ_e,

$$\xi = \frac{\text{apparent rate or current density}}{\text{intrinsic rate or current density}} = \frac{j_T}{alj(c_M^0, E^0)} \tag{27}$$

Table 2
Physical parameters used for the modeling.

Electrode parameters	References
Catalyst layer thickness, l (m)	
3.8×10^{-6}	[4]
5.0×10^{-6}	[32]
1.0×10^{-5}	[19,29]
2.3×10^{-5}	[18]
2.5×10^{-5}	[30]
5.0×10^{-5}	[13]
Specific area of anode, a (m^{-1})	
118,317	[29]
1.0×10^{5}	[17]
Porosity of anode, ε	
0.3	[31]
Diffusion coefficients, D_0 ($m^2\ s^{-1}$)	
$2.8 \times 10^{-9} \exp[2436((1/353)-(1/T))]$	[20,31]
1.6×10^{-9} (70 °C)	[18]
6.03×10^{-9} (60 °C)	[14]
Effective diffusion coefficients, D_e ($m^2\ s^{-1}$)	
$D_e = D_0 \varepsilon^{1.5}$	[6,18]
Effective conductivity, κ_e ($\Omega^{-1}\ m^{-1}$)	
3.4	[19,29]

Substituting Eq. (4) into Eq. (27), we have

$$\xi = \frac{j_T}{alj_0\theta^0_{OH,Ru}\theta^0_{CO}\ \exp(\beta E^0)} = \frac{J_T}{\theta^0_{OH,Ru}\theta^0_{CO}\ \exp(\Phi^0)} \quad (28)$$

Hence the relationship curves of j_T–ξ and J_T–ξ can be calculated for the Pt–Ru porous anode.

2.5. Numerical solution

The model Eq. (21) was solved by Newman's BAND (j) [6] based on a finite difference method. In each step, ΔX_i, a subroutine for solving a set of nonlinear algebraic equations was inserted to calculate the values of $\theta_{OH,Ru}(i)$ and $\theta_{CO}(i)$ which would be substituted into the source term [11]. Therefore all values of $\Psi(X)$ and $C_M(X)$ at nodes from 1 to $N+1$ can be obtained; namely the numerical solution of the model equation [7,11]. Once the model is solved, the polarisation curve as well as effectiveness factor can be obtained from the grads of $C_M(1)$ or $\Psi(1)$ according to Eqs. (25) and (28) [7,9].

3. Analysis of the macro-kinetics

In this paper, the physical parameters used are taken from the literature [4,6,13,14,17–20,29–32] and are listed in Table 2. Furthermore one set of kinetic parameters, corresponding to the elementary reaction steps, is regressed and listed in Table 3, which

Table 3
Kinetic parameters used for the model.

Kinetic parameters			
	30 °C	60 °C	90 °C
k_1 ($m\ s^{-1}$)	8.7×10^{-7}	4.2×10^{-6}	1.0×10^{-5}
k'_1 ($mol\ m^{-2}\ s^{-1}$)	4.0×10^{-4}	1.5×10^{-3}	2.6×10^{-3}
k_2 ($mol\ m^{-2}\ s^{-1}$)	3.5×10^{-9}	9.5×10^{-8}	8.0×10^{-7}
$k_{3,1}$ ($mol\ m^{-2}\ s^{-1}$)	–	3.2×10^{-9}	–
$k'_{3,1}$ ($mol\ m^{-2}\ s^{-1}$)	–	1.9×10^{-9}	–
$k_{3,2}$ ($mol\ m^{-2}\ s^{-1}$)	4.0×10^{-5}	5.0×10^{-5}	6.0×10^{-5}
$k'_{3,2}$ ($mol\ m^{-2}\ s^{-1}$)	3.0×10^{-5}	1.8×10^{-5}	1.4×10^{-5}
k_4 ($mol\ m^{-2}\ s^{-1}$)	5.3×10^{-2}	5.9×10^{-2}	6.2×10^{-2}
α_2		0.79	
β_3 (V^{-1})		0.5	
β_4 (V^{-1})		0.5	

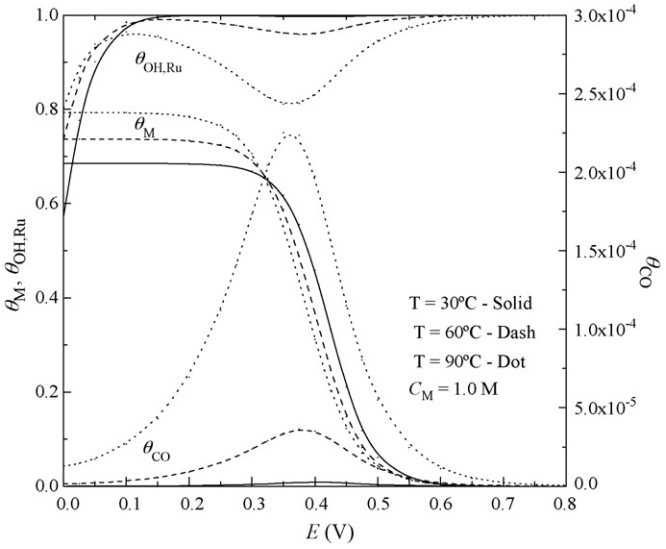

Fig. 2. Variations of coverage ratios with overpotential at different temperatures.

fit with the experimental polarisation data for bulk methanol concentrations 0.5 M, 1.0 M and 2.0 M ($mol\ dm^{-3}$) and temperatures of 30 °C, 60 °C and 90 °C, reported by Scott in Ref. [15].

3.1. Coverage ratios of species on the electrode surface

3.1.1. Variations of coverage ratios with overpotential

Generally the superficial rate or current density is proportional to both coverage ratios $\theta_{OH,Ru}$ and θ_{CO}, which are mutually coupled with the coverage ratio θ_M of CH_3OH_{ads} adsorbed at Pt sites. Also all of the coverage ratios are functions of concentration, temperature and overpotential.

Fig. 2 shows the variations of surface coverage ratios with overpotentials E, calculated by using the kinetics parameters at 30 °C, 60 °C and 90 °C with 1.0 M of methanol for Case A. The values for θ_M and $\theta_{OH,Ru}$ are shown on the left y-axis while values for θ_{CO} are shown on the right y-axis with a scale of 10^{-5}.

With increasing values of E, $\theta_{OH,Ru}$ rapidly increases to near 1, undergoes a slight decrease and, approaches 1 again: this means the electrochemical formation of OH at Ru site (step 3) may not become a rate limiting step. θ_M initially does not change with an increase in potential (maintains a value approximately that of the adsorption equilibrium) but then undergoes a sharp decrease, finally maintaining a small near constant value. This means that the adsorption rate of methanol (step 1) may be the rate limiting step with high overpotentials. However, values for θ_{CO} are always small; this means that the rate of surface reaction (last step 4) is much quicker than the rate of step 2. With increasing potential, θ_{CO} first shows a sharp increase and then undergoes a sharp decrease, ultimately maintaining very small values; this means that electrochemical dehydrogenation of CH_3OH_{ads} at Pt sites (step 2) may be the rate limiting step at low overpotentials. Hence there is no rate limiting step in the transition region with intermediate values of E.

In the model the influence of temperature on the coverage ratios is important. The activation energies, determined from Arrhenius plots of the rate constants (Table 2) with inverse temperature (not shown), of methanol adsorption of step 1 and of CH_3OH_{ads} dehydrogenation of step 2 were approximately 40 kJ mol^{-1} and 80 kJ mol^{-1} respectively. Looking back to Fig. 2, we can see that the greatest influence of temperature on the coverage ratios will take place in the case without a limiting step and that θ_{CO} is more sensitive to temperature than the other two coverage ratios; especially in the transition region. This indicates that the apparent activation energy

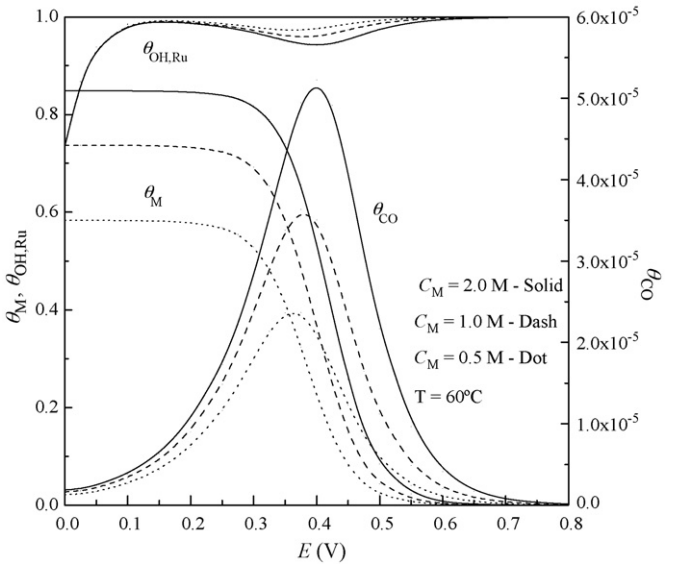

Fig. 3. Variations of coverage ratios with overpotential at different methanol concentrations.

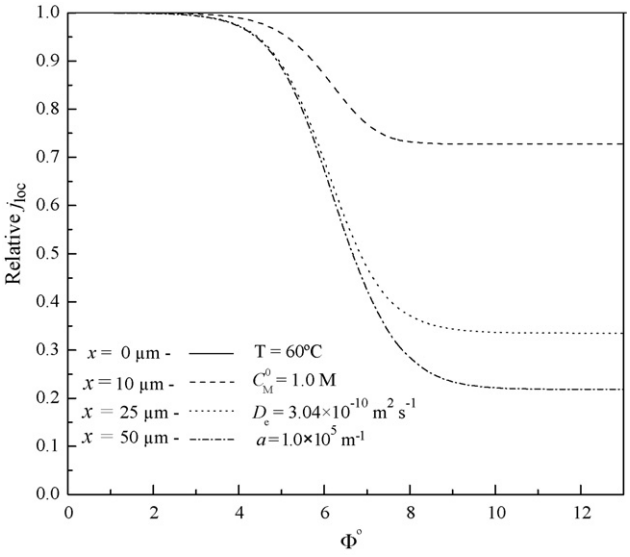

Fig. 4. Variation of distribution of relative j_{loc} with Φ^0.

in the transition region should be higher than that of any step of the series of elementary reactions; its maximum is equal to the sum of activation energies of all consecutive reactions, according to the kinetics of multistep reactions [22].

Fig. 3 shows the variation in surface coverages with potential at different concentrations for Case A at 60 °C. The values of θ_M appear to be more sensitive, and the values of $\theta_{OH,Ru}$ and θ_{CO}, less sensitive to concentration than to temperature. Similar to the trends in the data shown in Fig. 2, the rate limiting step will be step 2 at low E, then changes to step 1 at high E with increasing overpotential.

The current density of the limiting step 1 can be described approximately by a kinetic expression $j = nFk_1c_M^0$ (j is proportional to the bulk c_M^0) as the values of θ_M and θ_{CO} approach zero at high E, according to the rate expression for r_1 in Table 1 for Case A.

Theoretically, the last step, 4, of surface reaction producing CO_2 might be a rate limiting step under certain conditions such as high temperatures and concentrations, but not with the kinetic values adopted in this paper.

Overall, the rate limiting step may change from step 2, independent of concentration, and step 1, independent of overpotential, which will not only lead to a change in apparent activation energy but also to a change of reaction order between 0 and 1 with respect to methanol concentration. Furthermore it should be noted that θ_{CO} cannot be neglected since it is proportional to the total reaction rate, although its values are quite small. The sharp change of θ_{CO} as well as θ_M with overpotential is the reason that the kinetics of methanol oxidation on Pt–Ru cannot be simply described by B–V equations.

3.1.2. Distributions of coverage ratios in the porous anode

Spatial distributions in coverage ratios will exist in the porous anode, as the coverage ratios are functions of concentration, temperature and overpotential. Hence these distributions will also influence the local current density (or local reaction rate) distribution in the porous anode. Since the product $\theta_{OH,Ru}\theta_{CO}$ is directly proportional to surface current density, the distributions of $\theta_{OH,Ru}\theta_{CO}$ will have considerable influence on the local current density.

The variations in the relative local current density $j_{loc}(x)/j_{loc}(0)$ distributions with the dimensionless overpotential Φ^0 are shown in Fig. 4. This example was calculated by solving the macro-kinetic model equations at pore depth $x = 0\,\mu m$, $10\,\mu m$, $25\,\mu m$, $50\,\mu m$ respectively for a porous electrode of thickness $l = 50\,\mu m$. From the relative values of j_{loc} to the superficial $j_{loc}(0)$, it can be seen that $j_{loc}(x)$ is evidently impaired by coupled mass and charge transport for longer pores, at higher E.

A simpler way to solve the model equations for macro-kinetics is to take the product $(\theta_{OH,Ru}\theta_{CO})_{l=0}$ as independent of x and not a function of x; however this will bring considerable errors. By checking computations, the relative errors of local current densities j_{loc} $(\theta_{OH,Ru}\theta_{CO})_{l=x}/j_{loc}$ $(\theta_{OH,Ru}\theta_{CO})_{l=0}$ are, for example, from 20% to 50%, when, $x > 10\,\mu m$ and $\Phi^0 > 6.0$. Therefore it is important to involve the coverage ratio distributions in the analysis of macro-kinetics of the porous anode at most overpotentials.

3.2. Macro-polarisation curve and effectiveness

3.2.1. Macro-polarisation curve

The polarisation curve of a porous electrode, called the macro-polarisation curve, describes the variation in the applied surface overpotential E^0 and integral, total current density j_T.

Fig. 5a shows examples of the dimensional macro-polarisation curves corresponding to physical parameters arranged into five groups by 3 levels of electrode thickness, l, 2 levels of specific area, a and 1 level of effective diffusion coefficient, D_e. The parameters used for the curve numbered 4 (Fig. 5a) are very close to those used in Scott's papers [15,21]. All the macro-polarisation curves possess the same trend; an approximate exponential rise in current density with increasing overpotential and eventually approaching a maximum current density. This maximum current density is an "adsorption limiting current density", j_{al} rather than the familiar "limiting current density" caused by external mass transport.

The data show that thicker electrodes and higher specific electrode areas result in higher current densities at a given potential. The current densities are determined by the very low dehydrogenation rate of step 2 at low overpotentials as well as by the adsorption rate of step 1 at high overpotentials.

Fig. 5b shows the dimensionless macro-polarisation curves J–Φ^0 corresponding to the same physical parameters of Fig. 5a, and thus the dimensionless values of ν^2 and s. J is proportional to the mean value of current density per unit of inner surface area over the porous anode j_T/al, and therefore the J–Φ^0 curve shows the effects of mass and charge transfer on the porous anode. The curve with symbol △ represents the dimensionless intrinsic polarisation curve

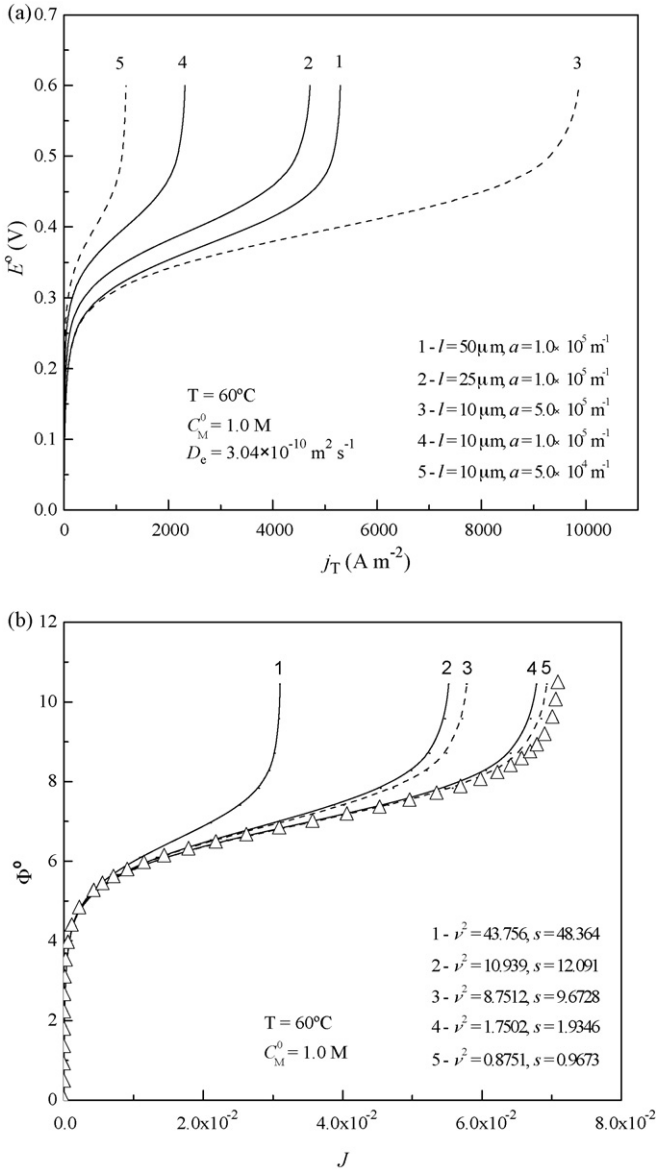

Fig. 5. (a) Macro-polarisation curves of j_T–E^0 for different a and l. (b) Dimensionless macro-polarisation curves J–Φ^0 for different ν^2 and s.

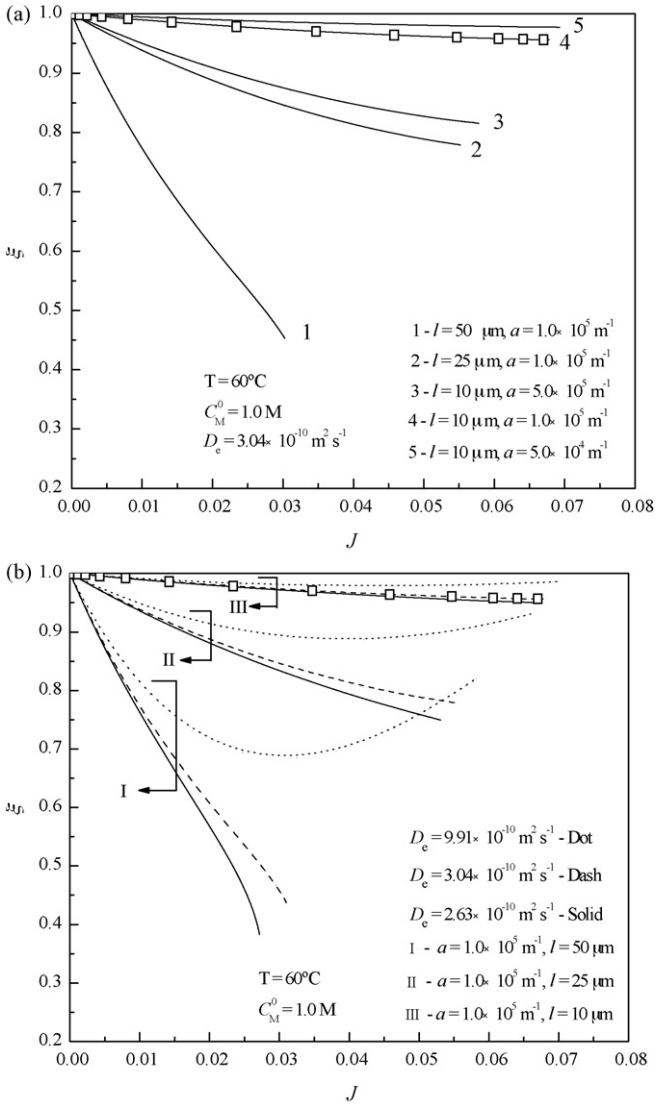

Fig. 6. (a) Variation of efficiency factor ξ with dimensionless current density J for different l and a. (b) Variation of effectiveness ξ with dimensionless current density J for different l and D_e.

independent of physical parameters, and can be calculated by the macro-model equation, but with $l \to 0$, say $l = 10^{-8}$ m, i.e. both ν^2 and $s \to 0$ in the numerical procedure.

The decreasing values of ν^2 and s corresponding to curves of 1, 2, 3, 4 and 5 result in higher current densities and indicate the decreasing influence of transport processes in the porous electrode. High values of ν^2 and s (approximately 40–50) for curve 1 have a large effect of transport while low values (<1.0) for curves 4 or 5 near the intrinsic curve (denoted by symbol △), had a slight effect. The physical parameters used for curve 4 are close to those in Scott's papers [15,21], which means that Scott's kinetic experiments were carried out under approximate intrinsic conditions.

3.2.2. Effectiveness of the porous anode

The effects of mass and charge transport can be characterised by the effectiveness ξ of the porous anode. The ξ–J curves calculated corresponding to the physical parameters in Fig. 5, are shown in Fig. 6a. The effectiveness is higher for thinner electrodes and for higher specific areas due to the decreasing influence of mass transport processes. With an increase in macro-current density, every point of the porous anode can undergo a change of limiting step from step 2 to step 1, depending on the local concentration and overpotential at the point. Therefore, the end point of each curve represents the dimensionless adsorption limiting current density, J_{al}, where only the effect of mass transport exists since the limiting step 1 is independent of overpotential. The data with symbol □ overlapping curve 4 (Fig. 6a) are calculated from the physical parameters used in Scott's papers [15,21]: all have values of ξ greater than 0.96, approaching a value of 1.0.

Theoretically the effectiveness is a function of both the effective diffusion coefficient D_e and conductivity κ_e characterizing both mass and charge transport in the porous anode. Fig. 6b shows the variations of ξ with D_e which essentially considers the effect of porosity ε of the anode, through for example the Bruggeman equation (i.e. $D_e = D_0\varepsilon^{1.5}$) [6,18]. The physical parameters are arranged into nine groups by three levels of electrode thickness, l, three levels of effective diffusion coefficient D_e and one level of specific area a. The three groups of curves, for the same value of D_e show the effects of ε and l on ξ. For a thinner porous electrode as well as a larger D_e, the influence of pore diffusion becomes

less significant, i.e. higher effectiveness values are achieved. Generally, effectiveness decreases with increasing macro-current density. However, for a thicker porous electrode as well as a larger D_e, effectiveness goes through a minimum with current density, which is caused by the effects of both mass and charge transport. With unceasingly increasing current density, the effect of charge transport resistance gradually disappears due to the change in the limiting reaction step (methanol adsorption). The effect of better mass transport, due to the larger D_e, means that more of the electrode would be operating at or close to a limiting current and hence effectiveness increases again as J increases, until J_{al} is reached.

4. Verification of the macro-kinetic model

4.1. Type of reaction mechanism

For model verification, the predicted macro-polarisation curves were compared to the experimental polarisation data reported by Scott or Nordlund's papers for methanol oxidation on the Pt–Ru porous anodes [15,16,18].

Fig. 7 shows two predicted macro-polarisation curves (solid lines 1 and 2), and two intrinsic polarisation curves (dashed lines 1′ and 2′), for the two kinetic models Case A (noted 1 and 1′) and Case B (noted 2 and 2′) respectively. The intrinsic polarisation curves were calculated by Eq. (3) $j = nF[-r_4(c_M^0, E^0)]$ and are independent of any physical parameters, which also consistent with those calculated by the macro-model equation but as the thickness approached the limit, $l \to 0$, in the numerical procedure. The experimental data, which are close to the model data for the intrinsic situation, from Scott's paper [15] are denoted by the symbol ○. The four curves only separate at high current densities due to the effects of transports or different mechanisms. The influence of the mechanism can be appreciated (see Fig. 8) from the differences in the variation surface coverages for the two mechanisms. Fig. 8 shows for Case B, the variation in coverage ratios with overpotential, using the kinetics parameters at 60°C at 1.0 M methanol. The main difference between the curves of Case B and Case A (Figs. 8 and 2) is that the coverage ratio $\theta_{OH,Pt}$ sharply increases at high overpotentials: this makes the polarisation curves turn back (decrease in current density) at high potentials due to the loss of Pt vacancy sites for methanol adsorption [15,18,23].

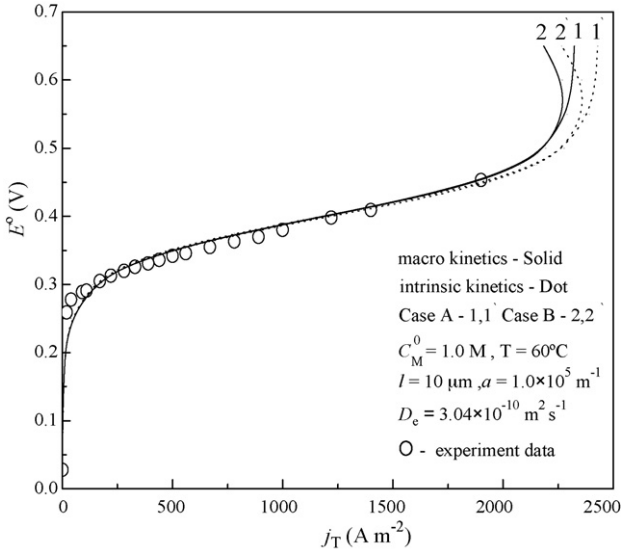

Fig. 7. Polarisation curves of j_T–E^0 for both Case A and Case B mechanisms.

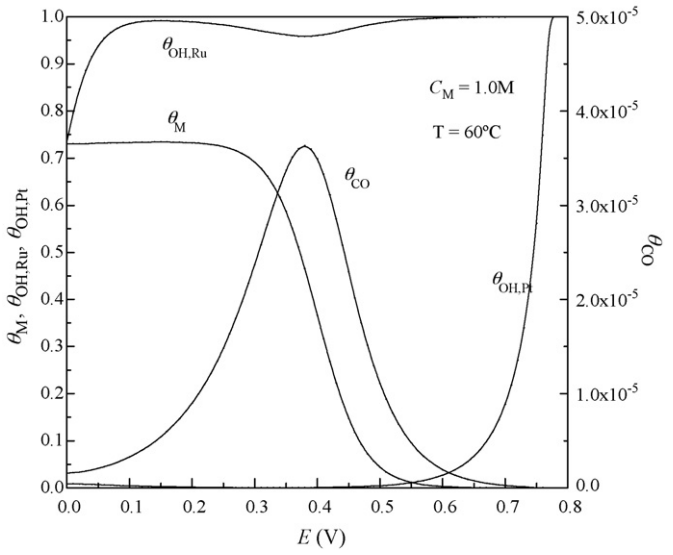

Fig. 8. Variations of coverage ratios (θ_M, $\theta_{OH,Ru}$, θ_{CO} and $\theta_{OH,Pt}$) with overpotential of mechanism Case B.

4.2. Effect of temperature and bulk concentration

Fig. 9a shows the predicted intrinsic (dashed lines) and macro-polarisation curves (solid lines) using at three temperatures: 30 °C, 60 °C and 90 °C. The experimental data from Scott and co-workers [15] are also shown for different temperatures. As expected increasing temperature increases current density. The data show again that Scott's kinetic experiments were carried out under approximate intrinsic conditions. The predicted values agree well with experimental data at lower currents at 30 °C and 60 °C, although there is a slight departure from the data at higher currents, which shows a linear trend, at 90 °C.

Fig. 9b shows the predicted intrinsic (dished lines) and macro-polarisation curves (solid lines) at 60 °C for three concentrations of methanol 0.5 M, 1.0 M and 2.0 M. The experimental data from Scott and co-workers [15] are indicated for different concentrations. The predicted values agree well with experimental data at lower current densities for 0.5 M and 1.0 M concentrations; however there is a considerable departure from the data at higher current densities at 2.0 M. The experimental current densities for a concentration of 2.0 M are lower than those predicted, and close to the data with $c_M^0 = 1.0$ M. A possible explanation for this may be that the effect of mass transport on the exterior surface of the porous anode becomes important at high currents as CO_2 bubbles may block methanol transfer from the bulk into the pores of the anode.

4.3. Effect of anode activity and thickness

Fig. 10a and b shows the predicted intrinsic (dished lines) and macro-polarisation curves (solid lines) for a porous anode with a higher activity and/or larger thickness. There are considerable differences between the intrinsic and macro-polarisation curves due to the influence of transport processes in the anode. Generally transport limitation decreases the current density from the anode at the same overpotential.

In Fig. 10a and b the experimental polarisation data reported by Nordlund and Lindbergh are shown [14,18]. Porous anodes prepared by different research groups may have different activities, microstructures, etc. The thickness (l = 23 μm) of the porous anode used to obtain the data [18] in Fig. 10b is approximately twice that (l = 14 μm) for the data in Fig. 10a [14]. Moreover the experimental current densities in Fig. 10a and b are greater than those of Scott

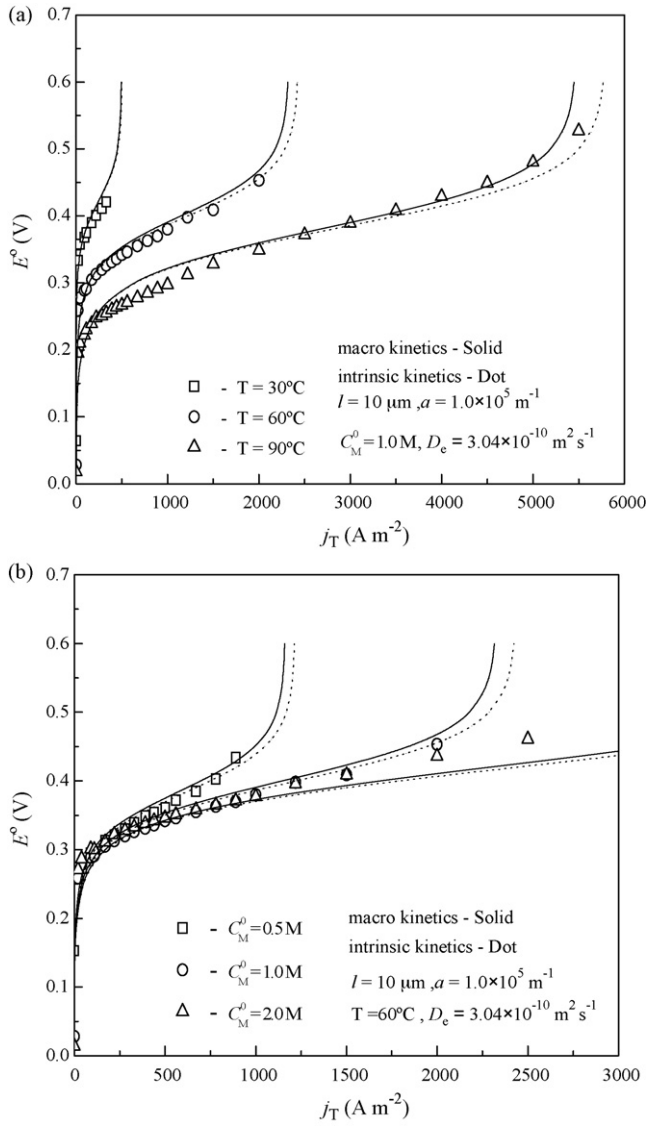

Fig. 9. Polarisation curves of j_T–E^0 for (a) different temperatures and (b) bulk concentrations of methanol.

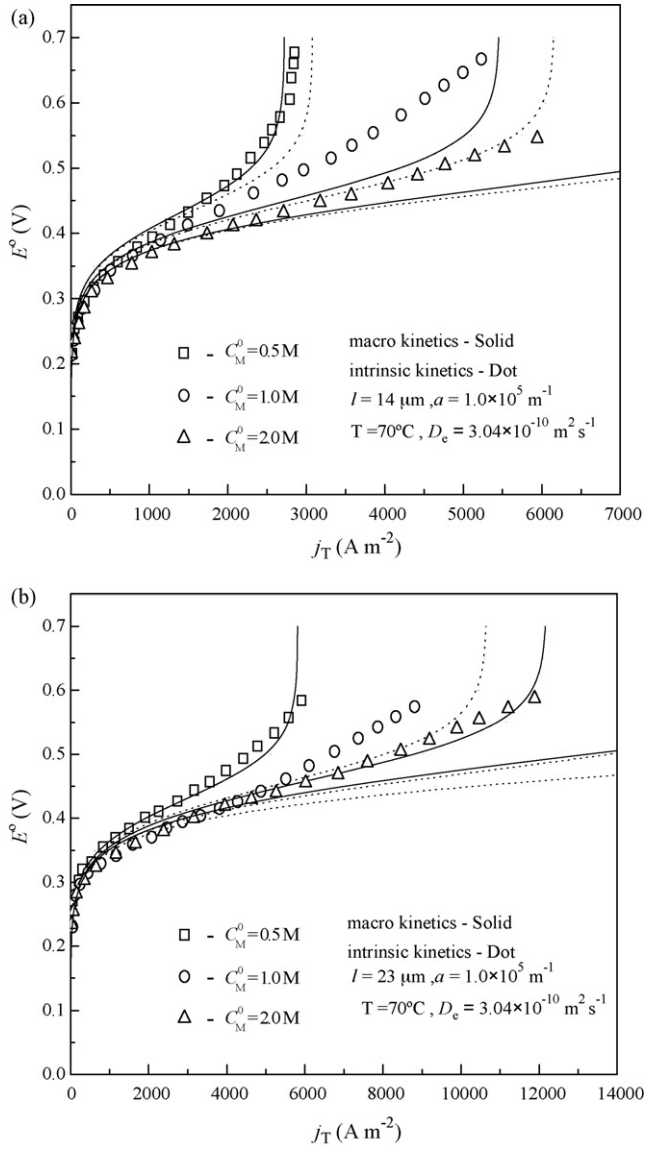

Fig. 10. Polarisation curves of j_T–E^0 for the anode with a (a) higher activity and (b) higher activity and a larger thickness.

and co-workers [15] in Fig. 9a and b. Hence we modified the values of kinetic parameters which are listed in Table 4 for the calculation of intrinsic and macro-polarisation curves at 70 °C.

In Fig. 10a, the data with c_M^0 of 0.5 M (denoted by symbol □), is consistent with the predicted macro-polarisation curve; however the data with c_M^0 of 1.0 and 2.0 M (denoted by symbols ○ and △) evidently depart from the corresponding predicted macro-polarisation curves at higher currents, i.e. the linear trend of the data. In Fig. 10b, for the porous electrode with a higher activity as well as a larger thickness, the data with c_M^0 of 1.0 M and 2.0 M are still consistent with the predicted macro-polarisation curves at lower currents, but depart considerably from the predicted macro-polarisation curves at higher currents. The data for 2.0 M methanol becomes much closer to that for 1.0 M and actually lie on the predicted macro-polarisation curve for 1.0 M.

As mentioned above, the macro-kinetic model developed here does not include the influence of two-phase flow caused by CO_2 bubbles, which impede methanol transport. Thus is likely that the departure of experimental data from the predicted data, tending to be linear at higher currents, may be that the electrode polarisation here is dominated by concentration polarisation caused by mass transfer limitations of two-phase flow rather than the kinetic polarisation at higher currents as more CO_2 is produced.

Table 4
Kinetic parameters based on Ref. [15] at 70 °C.

	l = 14 μm	l = 23 μm
k_1 (m s^{-1})	7.6 × 10^{-6}	1.6 × 10^{-5}
k_1' (mol m^{-2} s^{-1})	2.5 × 10^{-3}	2.5 × 10^{-3}
k_2 (mol m^{-2} s^{-1})	5.8 × 10^{-8}	5.8 × 10^{-8}
$k_{3,2}$ (mol m^{-2} s^{-1})	5.5 × 10^{-5}	5.5 × 10^{-5}
$k_{3,2}'$ (mol m^{-2} s^{-1})	1.3 × 10^{-5}	1.3 × 10^{-5}
k_4 (mol m^{-2} s^{-1})	6.1 × 10^{-2}	6.1 × 10^{-2}

5. Conclusion

A macro-kinetic model of a porous Pt–Ru anode for methanol oxidation has been developed. The performance of the porous Pt–Ru anode depends on the mechanism and parameters of the intrinsic kinetics of methanol oxidation as well as parameters such as thickness of the electrode, surface area, effective diffusion, charge transfer coefficients, etc.

Intrinsic kinetics of the oxidation are only related to the flux of charge on the surface of porous electrode, i.e. the current density being independent of any physical parameter, but macro-kinetics are related to the divergence of current density in the volume of the porous electrode, the latter requires a set of second order differential equations to describe the coupled physical transport process and chemical reaction processes in a three dimension space.

The mathematical model of macro-kinetics, developed, has two traits: firstly it contains the dual-site mechanism of methanol oxidation on Pt–Ru anode; secondly the model equations are generalized.

By using the finite difference method with a subroutine for solving a set of nonlinear algebraic equations in each step, the solutions of the model, the distributions of concentration and overpotential, were obtained as well as the surface coverage ratio distribution, effectiveness of the porous electrode and macro-polarisation curves.

Comparing the predicted polarisation curves with experimental polarisation data, the theoretical analysis for the performance of the porous anode can be carried out to understand macro-kinetics as well as to find out ways to improve the performance of the electrode.

From the theoretical analysis, the apparent current densities are very small and almost approach zero at low overpotentials for all cases since the dehydrogenation rates of CH_3OH_{ads} adsorbed on the Pt sites are too small. Therefore improving the electrocatalyst activity is an important issue [24,25] for reducing the considerable electrode polarisation near "open-circuit". Comparing the kinetic parameters in Table 3 with those in Table 2, it seems that the capacity of the Pt–Ru anode for methanol oxidation is actually limited by the rate of methanol adsorption on the Pt sites; hence to accelerate the adsorption on the electrocatalyst is another important issue.

The predicted polarisation curves calculated by the model of macro-kinetics without taking into account two-phase flow, are consistent with experimental polarisation data at lower current densities. This feature implies that the porous electrode, with a high specific area for higher apparent current density at lower local current density, will be instrumental in reducing the influence of two-phase flow. The departure of experimental data from the predicted polarisation curves at high concentration at high apparent current densities is likely due to the two-phase flow mode. Optimising the electrode structure in relation to the two-phase flow is also an important issue for further investigation [26–29].

This work also can be referenced for theoretical analyses of porous or packed bed anode in other Direct Liquid-Feed Fuel Cell, using other alcohols, borohydride, etc.

Acknowledgement

The authors acknowledge the support of research project NSFC (20776091) provided by China National Natural Science foundation.

References

[1] K. Scott, A. Shukla, in: R.E. White (Ed.), Modern Aspects of Electrochemistry, No. 40, Springer, New York, 2007, pp. 127–228.
[2] B. García, J. Weidner, in: R.E. White (Ed.), Modern Aspects of Electrochemistry, No. 40, Springer, New York, 2007, pp. 229–284.
[3] S. Gottesfeld, J. Power Sources 171 (2007) 37–45.
[4] J. Meyers, J. Newman, J. Electrochem. Soc. 149 (6) (2002) A718–A728.
[5] J. Newman, C. Tobias, J. Electrochem. Soc. 109 (12) (1962) 1183–1191.
[6] J. Newman, Electrochemical Systems, third ed., Prentice-Hall, New Jersey, 2004.
[7] K. Scott, Y.-P. Sun, in: C. Vayenas, M. Gamboa-Adelco (Eds.), Modern Aspects of Electrochemistry, No. 41, Springer, New York, 2007, pp. 221–304.
[8] Y.-P. Sun, K. Scott, Fuel Cell 4 (1/2) (2004) 30–38.
[9] Y.-P. Sun, K. Scott, Chem. Eng. J. 1024 (1) (2004) 83–91.
[10] Y.-P. Sun, J. Chem. Ind. Eng. 58 (9) (2007) 2161–2168 (in Chinese).
[11] Y.-P. Sun, L. Xing, CIESC 60 (1) (2009) 55–68 (in Chinese).
[12] H. Gasteiger, N. Markovic, P. Ross Jr., J. Cairns, J. Phys. Chem. 97 (1993) 12020–12029.
[13] P. Kauranen, E. Skou, J. Munk, J. Electroanal. Chem. 404 (1996) 1–13.
[14] J. Nordlund, G. Lindbergh, J. Electrochem. Soc. 151 (9) (2004) A1357–A1362.
[15] M. Shivhare, R. Allen, K. Scott, A. Morris, E. Martin, J. Electroanal. Chem. 595 (2006) 145–151.
[16] M. Shivhare, C. Jackson, K. Scott, E. Martin, J. Power Sources 173 (2007) 240–248.
[17] B. García, V. Sethuraman, J. Weidner, R.E. White, R. Dougal, J. Fuel Cell Sci. Technol. 1 (2004) 43–48.
[18] J. Nordlund, G. Lindbergh, J. Electrochem. Soc. 149 (9) (2002) A1107–A1113.
[19] K. Scott, P. Argyropoulos, J. Power Sources 137 (2004) 228–238.
[20] K. Scott, W. Taama, S. Kramer, P. Argyropoulos, K. Sundmacher, J. Electrochim. Acta 45 (1999) 945–957.
[21] K. Scott, P. Argyropoulos, K. Sundmacher, J. Electroanal. Chem. 477 (1999) 97–110.
[22] F.G. Helfferich, Kinetics of Multistep Reactions, Elsevier, Amsterdam, 2004.
[23] P. Kauranen, E. Skou, J. Munk, J. Electroanal. Chem. 404 (1996).
[24] N. Tian, Z.-Y. Zhou, S.-G. Sun, Y. Ding, Z.-L. Wang, Science 316 (5825) (2007) 732–735.
[25] Q. Wang, G.Q. Sun, L. Gao, L.H. Jiang, G.X. Wang, S.L. Wang, S.H. Yang, Q. Xin, J. Power Sources 177 (2008) 142–147.
[26] J. Nordlund, C. Picard, E. Birgersson, M. Vynnycky, G. Lindbergh, J. Appl. Electrochem. 34 (2004) 763–770.
[27] R. Allen, L. Chan, L.-X. Yang, K. Scott, S. Roy, J. Power Sources 143 (2005) 142–149.
[28] R. Chetty, K. Scott, J. Electrochim. Acta 52 (2007) 4073–4081.
[29] K. Scott, P. Argyropoulos, J. Electroanal. Chem. 567 (2004) 103–109.
[30] L. Chan, R.G. Allen, K. Scott, J. Power Sources 161 (2006) 11–18.
[31] K. Scott, W. Taama, J. Cruickshank, J. Power Sources 65 (1997) 159–171.
[32] Z.G. Shao, W.F. Lin, F.Y. Zhu, P.A. Christensen, M.Q. Li, H.M. Zhang, J. Electrochem. Commun. 8 (2006) 5–8.